

Magnetically bistable actuator Part 2. Fabrication and performance

Gary D. Gray Jr.^a, Eric M. Prophet^b, Lingbo Zhu^a, Paul A. Kohl^{a,*}

^a School of Chemical Engineering, Georgia Institute of Technology, 311 Ferst Dr., Atlanta, GA 30332-0100, USA

^b Superconductor Technologies, Inc., Santa Barbara, CA, USA

Received 26 July 2004; received in revised form 19 October 2004; accepted 21 October 2004

Available online 8 December 2004

Abstract

A bistable magnetic MEMS actuator was fabricated using microelectronic processes including a two-substrate flip-chip assembly, multilevel metallization, and sublimation release to avoid stiction. The actuator was found to have excellent correspondence between observed and modeled behavior. The benefits of shape anisotropy are quantified. Lithographic patterning of the magnetic material into long narrow strips along the actuator's length resulted in much greater magnetic torques being developed at reduced external field levels. Low levels of anisotropy led to designs with low levels of magnetization and therefore required higher external magnetic fields, whereas high levels of anisotropy led to designs latching at 10 mT levels with contact forces greater than 5 μ N with switching energies less than 100 μ J and a switching speed of less than 5 ms. More moderate levels of anisotropy resulted in a design space where <1 μ J switching energies could be realized. Electrical performance has been demonstrated over 2 million cycles, and mechanical performance to 150 million cycles. Applications include electronics, microfluidics, and cryogenic devices.

© 2004 Elsevier B.V. All rights reserved.

Keywords: Single pole double throw; Radio frequency; Short-pulse switching

1. Introduction

In Part 1, the design space was analyzed for bistable magnetic actuators with minimal power consumption and reasonable contact force subject to a 100 μ m actuation distance [1]. The test vehicle we used to evaluate this type of actuator was a single pole double throw (SPDT) radio frequency (RF) switch since many of the design features we have optimized and would like to examine are inherent in this type of device [2]. The device was constructed between two low-loss alumina substrates, flip-chip bonded together. The magnetic actuator forms a cantilever, which is doubly hinged to a post attached to the lower substrate. The post extends 30 μ m above the lower substrate. The actuator provides a transmission path to switch between the two microstrip transmission lines on either substrate [2]. With the exception of the thin

layer of Sn/Pb solder bonding the connection posts between the two substrates, the entire electrical signal path, including the posts, hinges, and contact pads are fabricated of gold. The ferromagnetic element of the beam is clad on both sides with 3 μ m of gold to reduce thermal-induced bending and improve electrical performance. The offset of the two substrates is determined by the post height and solder thickness. The switching coil is located on the outside of the two-substrate assembly and is shielded by means of a ground plane to avoid any pick-up of the RF signal in the actuation coils. The devices were designed and modeled previously [1]. In this paper, different switching mechanisms are explored, including the short-pulse switching (SPS) modeled before [1]. In addition, the method of fabrication and the electrical and mechanical performance are investigated. Finally, potential applications of the devices, aside from the high-isolation low-loss RF SPDT switch described in this paper, will be presented.

* Corresponding author. Tel.: +1 4048942893; fax: +1 4048942866.

2. Theory

According to the analysis presented in [1], the short-pulse switching (SPS) regime requires a much smaller overall actuation energy but requires a larger magnetic field (greater coil current) than the long-pulse switching for a complete switching event to occur. That is, after the short-pulse is provided, some reversed magnetization, M_{critical} , must remain in the Ni/Fe in order to complete the switching event without any additional assistance from the coil. The minimum degree of magnetization that must be generated by the external coil to satisfy the SPS conditions must also satisfy the following, Eq. (1), which follows from rearrangement of Eq. (19) from Part I.

$$B_{\text{coil}} \cos \varphi > B_{\text{external}} \sin \varphi + H_c + \sqrt{N_L^2 + \theta^2} M_{\text{critical}} \quad (1)$$

where B_{coil} is the magnetic field produced by the coil, φ the angle of inclination of the beam with respect to a given substrate, H_c the coercivity of the permalloy, N_L the length demagnetization factor of the permalloy, B_{external} the background magnetic field, and θ the angle the magnetization vector is rotated out-of-plane of the magnetic element. This required magnetic field for SPS exceeds the required magnetic field for long-pulse switching (given by Eq. (1) in Part I) by the following quantity.

$$\Delta B_{\text{coil}} \cos \varphi > \sqrt{N_L^2 + \theta^2} \left(\frac{\Gamma_{\text{elastic}}}{V B_{\text{external}}} + M_{\text{critical}} \right) \quad (2)$$

where V is the volume of the magnetic material, and Γ_{elastic} is the elastic torque at the initial stable or latched position.

The minimum magnetization that must be realized in order for the SPS to succeed can be obtained through graphical analysis of the minor hysteresis loops of permalloy. Fig. 1 depicts the major hysteresis loop of a ferromagnetic material

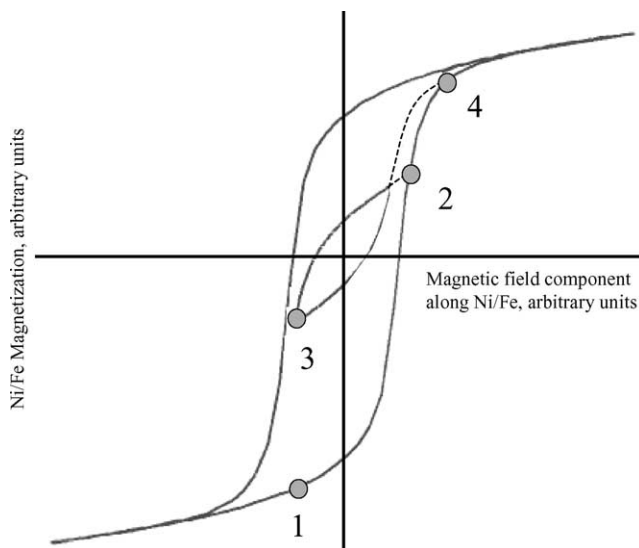


Fig. 1. Hysteresis curves of a soft ferromagnetic material, depicting multiple path-dependent magnetization values at a given background magnetic field.

in which the magnetization ranges from saturated in an initial direction to saturated in the opposite direction and back. Additionally, an example minor hysteresis loop is shown, which is followed whenever the magnetic field is diminished before achieving saturation. Assume the beam is initially in the downstate ($M < 0$) with magnetization given by point 1. A short current pulse is then supplied to the integrated coil, momentarily moving the magnetization along the bottom curve to point 2. Once the coil current is terminated, the magnetization will travel along a minor hysteresis loop to point 3, until reaching the same level of external field as initially in point 1. If the magnetization magnitude is sufficiently reduced so that the magnitude of the magnetic torque is now less than the elastic torque, the device will switch; during switching, the magnetization will again increase due to the ever-increasing external field component along the permalloy beam. Once point 2 is passed, the magnetization will closely follow the major hysteresis loop (resulting in point 4). Through this figure, it can be seen that only a small value of the magnetization must be developed opposite the original direction in order for the remnant magnetization to closely follow the major hysteresis loop. In fact, if M_{critical} is small compared to $\Gamma_{\text{elastic}}/(V B_{\text{external}})$, M_{critical} may be neglected. This allows for an approximate value of ΔB_{coil} , and therefore an increase in current, ΔI , to be calculated. Although a somewhat larger current must be applied, a great reduction in switching energy may be realized, as the time for magnetic realignment is much shorter than half the transient switching time.

In the remainder of this paper we will show that the minimum switching energy necessary to create a complete switching event can be anticipated and achieved by optimizing the demagnetization of the permalloy beam and the hinge stiffness. In order to test the validity of the optimization method, a simple two-substrate switch was fabricated using the optimized magnetic actuator to toggle between the microstrip transmission lines on opposing substrates. The following section details an exemplary fabrication process used to realize such a switch.

3. Experimental

3.1. Top substrate processing

The top alumina substrate is cleaned with a standard 5% H_2SO_4 + 2% H_2O_2 /1% ammonia/acetone/isopropanol sequence. The seed layer for the upper ground plane is DC sputtered with 200 Å of Ti, followed by 4 μm of Cu and 200 Å Ti (shown in Fig. 2) which forms the ground plane. A 5 μm benzocyclobutene (BCB) film is then spun and cured as an isolation barrier between the ground plane and actuation coil. Next, 200 Å of Ti and 1800 Å Au is DC sputtered as seed layer above the BCB to form the actuation coil. A 4 μm of soft gold is then electroplated at a current density of 5 mA/cm², a bath temperature of 50 °C, and a 600 rpm stir rate. AZ460 resist is spun on for 10 μm thickness, baked on a hot plate at 90 °C for

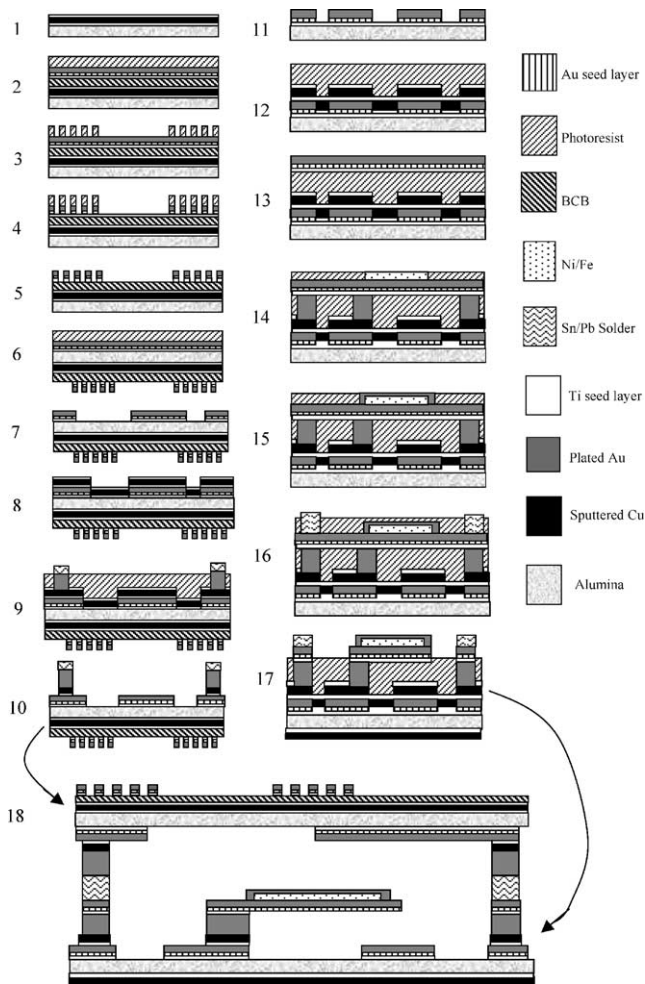


Fig. 2. Process flow schematic for dual-substrate design.

15 min, aligned to mask 1 to pattern the actuation coil, and exposed for 70 s for a total dose of 900 mJ/cm^2 (Fig. 2, 1). The resist is developed in AZ400K at a ratio of 1 part AZ400K to 4 parts DI water for approximately 3 min (Fig. 2, 3). The AZ resist is a positive tone resist, so the exposed regions are removed by the developer solution. Gold is etched for about 7 min in KI/I_2 solution to form the coils (Fig. 2, 4), and the photoresist is stripped in acetone. The exposed Ti seed layer is also stripped (Fig. 2, 5). The substrate is flipped over. The seed layer for the microstrip transmission line is deposited by DC sputtering 200 \AA of Ti, followed by 2000 \AA of Au. Next, 4 \mu m of soft gold is electroplated to form the metal layer for the microstrip transmission line. AZ4620 resist is spun and exposed through mask 2, aligned to the previously patterned backside of the alumina substrate (Fig. 2, 6). After the photoresist has been patterned with the microstrips, Au and Ti are etched; and photoresist is stripped (Fig. 2, 7). The Au microstrips, along with the Au ground plane on the opposite side, will form the transmission lines. The next step is to plate up the tall posts which will act as standoffs to provide adequate substrate separation. A 150 \AA Ti is electron beam deposited, followed by 2000 \AA Cu and 150 \AA of Ti (Fig. 2,

8) to be used as an electrical bus for electroplating. A thick 30 \mu m layer of AZ4620 is spun onto the substrate and baked on a hot plate at $90 \text{ }^\circ\text{C}$ for 20 min. The substrate is aligned to mask 3, and the photoresist is exposed for a total dose of 1550 mJ/cm^2 and developed to form the upper post vias. The Ti layer is removed with a 20 s dip in buffered oxide etch (BOE). The upper posts are formed by electroplating 30 \mu m of soft gold using the same conditions as before. This requires about 100 min electroplating time. Sn/Pb solder is used as a bonding medium and is electroplated above the 30 \mu m gold using a pulsed bath at a current density of 5 mA/cm^2 (Fig. 2, 9). The photoresist is stripped in acetone, and the top substrate is placed aside during the processing of the bottom substrate (Fig. 2, 10).

3.2. Bottom substrate processing

The bottom alumina substrate is cleaned with a standard $5\% \text{ H}_2\text{SO}_4 + 2\% \text{ H}_2\text{O}_2 + 1\% \text{ ammonia/acetone/isopropanol}$ sequence. A 200 \AA of Ti and 1800 \AA gold are DC sputtered as a seed layer for the lower layer transmission lines. The microstrip transmission line metal layer is formed with 4 \mu m of soft gold, which is electroplated at a current density of 5 mA/cm^2 at a bath temperature of $50 \text{ }^\circ\text{C}$ and 600 rpm stir rate. AZ460 resist is spun on for 10 \mu m thickness, baked on a hot plate at $90 \text{ }^\circ\text{C}$ for 15 min, and aligned to mask 4. Gold is etched and photoresist is stripped, as shown in Fig. 2, forming the transmission lines. Next the tall standoff posts and anchors are deposited. A 150 \AA Ti, followed by 2000 \AA Cu and 150 \AA Ti using electron beam evaporation. (Note: the Cu here is to act as a seed layer and electrical bus for the post and beam electroplating on the bottom substrate. A different metal is required so as to not lose the microstrips already patterned in Au.) A 30 \mu m thick layer of AZ4620 is spun onto the substrate and baked on a hot plate at $90 \text{ }^\circ\text{C}$ for 20 min (Fig. 2, 12). Mask 5 is aligned, and the resist is exposed for a total dose of 1550 mJ/cm^2 and developed, forming the post vias. The Ti layer at the bottom of the vias is removed with a 20 s dip in BOE to provide adequate adhesion of the posts with the substrate. The lower posts are formed by depositing 30 \mu m of soft gold using the same electroplating conditions as before (Fig. 2, 13). This 30 \mu m photoresist is not removed and is instead used as a sacrificial layer for subsequent processing. A 150 \AA of titanium is electron beam deposited, followed by 1500 \AA gold, as a seed layer for beam formation, and 2 \mu m of soft gold is electroplated using the same conditions as in top substrate processing. Note this thickness of soft gold will be the thickness of the cantilever hinges. AZ4620 is coated a second time (10 \mu m) and exposed through mask 6 at a dose of 900 mJ/cm^2 to form the permalloy mold. After the resist is developed, 12 \mu m of permalloy is selectively electroplated using a current density of 17 mA/cm^2 for 20 min (Fig. 2, 14). The permalloy bath composition was given by Ahn and Allen [3]. The top photoresist is then stripped with acetone. An additional layer of gold is then deposited over the lossy permalloy to improve the thermal and electrical properties of

the device. The upper Au layer mold is then patterned with a 10 μm AZ4620 resist layer and exposed through mask 7 for 75 s, for a total dose of 1000 mJ/cm^2 . After the resist is developed, the 2 μm soft gold upper layer is selectively electroplated over the permalloy, and then the photoresist is stripped (Fig. 2, 15). Next a layer of Sn/Pb covering the standoff posts is needed to form a low-temperature eutectic bond between the two substrates. To accomplish this, an AZ4620 resist layer is spun on for 10 μm , aligned and exposed through mask 8 and developed. A 8 μm of Sn/Pb solder is electroplated using same bath and conditions as found in top substrate solder electroplating (Fig. 2, 16). The final step is to pattern the multi-metal stack in the photoresist to form the RF switches. This is done by spinning 10 μm of AZ4620 and exposing through mask 9 for 70 s, for a total dose of 900 mJ/cm^2 . The entire gold stack is then etched for about 7 min in KI/I_2 solution. Constant agitation is necessary. After the beam material has been etched, the Ti layer is removed with 15 s dip in BOE, and the top photoresist is stripped in acetone. Lastly, a 100 \AA Ti seed layer and a 4 μm ground plane layer are sputtered on the backside of the wafer to complete the lower substrate microstrip waveguide (Fig. 2, 17).

Both alumina substrates are then diced, and in order to avoid stiction in the release process the devices are released according to the following steps: the 30 μm thick photoresist layer is stripped with acetone; the Ti layer is removed with a 15 s BOE dip; the Cu seed layer is etched with 5% acetic acid/2% H_2O_2 solution; the bottom Ti layer is removed with a 20 s BOE dip; devices are then soaked in acetone. Released beams are then transferred from acetone to clean cyclohexane. Dies are individually removed from cyclohexane, and after removing excess cyclohexane, are placed in a cool (0 $^\circ\text{C}$) nitrogen-purged thermos directly above an external magnet. The devices are allowed to warm slowly, resulting in sublimation of the cyclohexane. Once the cyclohexane in contact with the cantilever beam has sublimed, the beam bends out of plane and stiction-free release of the devices is achieved. Mating pieces are then aligned and brought into contact using a Flip-Chip Bonder. The solder is heated and flows, bonding the pieces together (Fig. 2, 18).

4. Results

The Fig. 3a and b depict a device in the up and down states, respectively. The top substrate is not in place so that the interior of the assembly may be seen clearly. Fig. 3a shows the released beam in the up state above the alumina substrate.

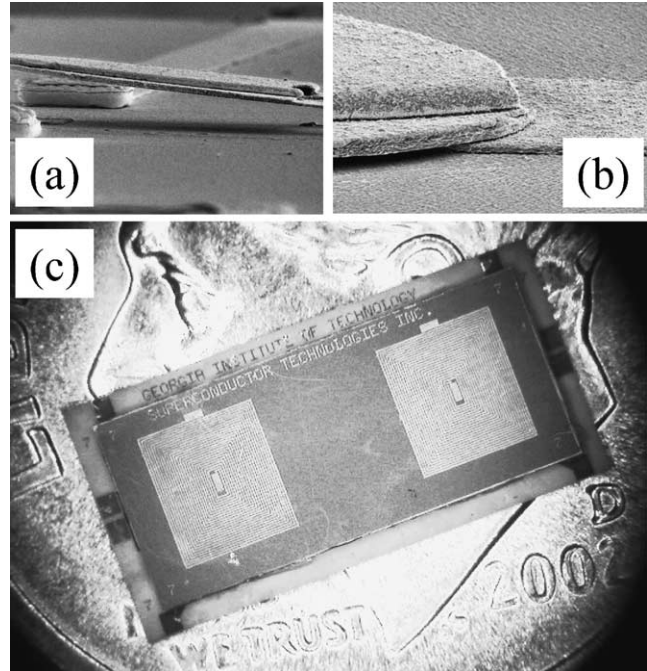


Fig. 3. Individual MEMS actuators in (a) upstate, (b) downstate, and (c) assembled (size compared to standard 17.9 mm U.S. dime).

The device is anchored to a post on the right (not shown). Two similar posts are shown, one each in the foreground and background. Fig. 3b shows the same device in the down state, in contact with a microstrip line on the alumina substrate. The completed two-substrate assembly is shown in Fig. 3c. The upper substrate, with the printed coils exposed, is slightly smaller than the underlying bottom substrate. This is done so that wire bonding can easily be performed to the exposed contact pads on the perimeter of the bottom substrate. The completed chip shown measures 10 mm \times 5 mm and contains two independent microelectromechanical systems (MEMS) SPDT switches forming a transfer switch, each with its own switching coil.

Three different devices were built to match the three designs described previously [1]. The devices that were fabricated are summarized in Table 1 of Part I. Designs 1 and 3 have longer beams with several patterned Ni/Fe strips, while design 2 is a shorter device with a single Ni/Fe section. Previous work predicted design 1 to have a 7 μN contact force at a background 10 mT magnetic field, whereas design 2 has a contact force about 4 μN in a 25 mT external magnetic field. Greater contact forces are achieved with larger background fields, with contact forces increasing as B^2 for designs with

Table 1
Comparison of modeled and experimental data for minimum conditions

Minimum conditions	Design 1	Design 2	Design 3
Modeled	1.3 mT external field; 0.35 mT from coil; 26 mA to coil	20 mT external field; 1.5 mT from coil; 90 mA to coil	4.0 mT external field; 0.40 mT from coil; 30 mA to coil
Experimental	1.5 mT external field; 0.40 mT from coil; 30 mA to coil	20 mT external field; 1.7 mT from coil; 100 mA to coil	7 mT external field; 0.45 mT from coil; 35 mA to coil

low anisotropy (design 2) and increasing with B for designs with high shape anisotropy (designs 1 and 3). Reduced field levels were used to facilitate low-energy switching. Design 2 was predicted to switch more quickly than the others, owing to reduced mass and greater driving torque during switching (proportional to B_{ext}), but with a greater energy expenditure. Design 3 was designed to be a compromise between the first two designs and yielded SPS.

4.1. Modeling comparison

Before comparing modeled and experimental dynamic operation, static response was examined to ensure accurate determination of magnetic volume, hinge stiffness, coercivity, and shape anisotropy. The response of the devices to external magnetic fields was tested above a calibrated electromagnet. Devices were tested in air at ambient conditions without an upper substrate. Field levels were confirmed with a handheld GMW, Inc. Hall Teslometer. The response of all three designs to external magnetic fields is presented in Fig. 4. The initial inclination angle of each cantilever is the y -intercept value. A gradual increase in angular position of the beam is seen with application of low magnetic field. As the external field is raised, the beam moves more easily as a greater component of the external field lies along the beam length, producing a higher level of magnetization and therefore a greater magnetic torque. Eventually the magnetization of the beam becomes saturated, and experiences a slow asymptotic approach to $\pi/2$. For devices 1, 2, and 3, saturation appears to occur at 3 mT (point 1 s), 22 mT (point 2 s), and 6 mT (point 3 s), respectively, as shown in Fig. 4. Note that these data follow the trends predicted by increased shape anisotropy and permalloy volume; that is, the designs with smaller length demagnetization factors and greater permalloy volume have resultingly lower saturating external magnetic fields. Each area of these characteristic curves reflects a different combination of the above-mentioned factors. For instance, the onset of saturation is most strongly influenced by the combination of demagnetization, background magnetic field, and

hinge stiffness. The behavior above saturation, however, is dominated by the relative magnitude of the hinge stiffness and magnetic volume; low-field level behavior is influenced by the coercivity, demagnetization, and initial beam deflection. Excellent agreement between modeled and experimental behavior close to and above saturation permitted variation of the coercivity parameter until a best-fit value of 0.3 mT (250 A/m) was obtained for each device design. This value is well in line with previously reported data [4]. It should be noted that the coercivity is a critical parameter for successful SPS. Low values of coercivity bring the $+H_c$ and $-H_c$ magnetic torque curves close together, virtually eliminating the possibility for SPS by reducing the range of hinge stiffness giving elastic torques bound by the magnetic torque and further diminishing the contact force available. Higher values of coercivity increase the potential for SPS and increased contact force, but due so by drastically increasing the magnitude of the current necessary for the short-pulse, representing an increase in the cost of thermal management.

The effect of reduced length demagnetization factor (the N_L value) on the characteristic curve shown in Fig. 4 is quite large between devices 2 and 3, but the difference is less so between devices 3 and 1. This is explained by the increasing impact of θ in the denominator of Eq. (7) in Part 1 [1]. As the length demagnetization factor, N_L , decreases in going from device 2 to 3 and 1, θ is no longer dominated by N_L . In fact, while θ is negligible over the entire angular range of interest for the limited shape anisotropy in design 2, for both designs 1 and 3, θ is the dominant factor in determining the approach to saturation. This difference shown in Fig. 4 between devices 1 and 3 is due to the larger permalloy volume of device 1 (producing a larger magnetic torque in a given magnetic field, resulting in a greater beam angular deflection for the same hinge stiffness, producing a larger permalloy magnetization, etc.).

Devices were modeled according to the static model used by Judy and Muller [4], and detailed in Ref. [1]. Deflection data for the devices were taken at a variety of magnetic field strengths, and these data were converted into inclina-

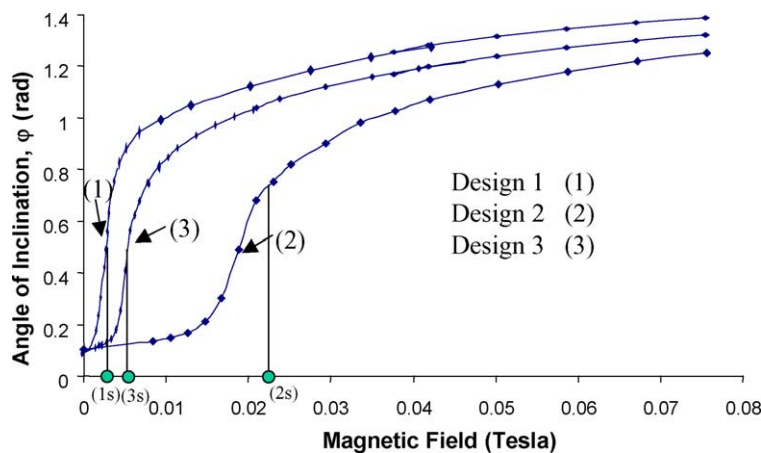


Fig. 4. Observed characteristic deflection curves for three actuator designs, depicting behavior above and below saturation.

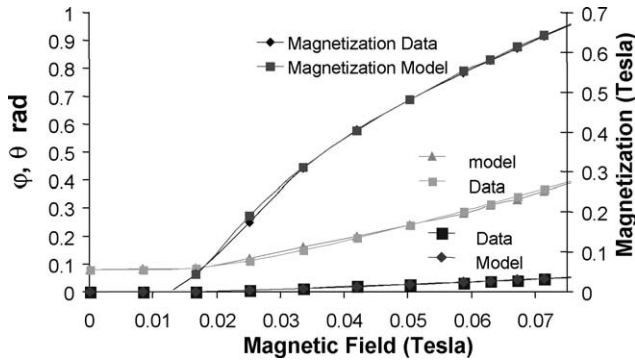


Fig. 5. Comparison of modeled and experimental data for a type-2 device with $3 \mu\text{m}$ thick gold hinges.

tion angles of the cantilevers. The magnetization data was calculated from the observed deflections using the known geometry of the permalloy and hinges, as well as the demagnetization factors calculated from the permalloy shape. The observed inclination angle and calculated magnetization data are compared to the modeled inclination angle and modeled magnetization data for the same device. As previously demonstrated by Judy and Muller, inclusion of the anisotropy torque in the static analysis greatly increases the correspondence between the model and observed behavior (particularly at low-field levels [4]), as shown in Fig. 5, in which a type-2 device with $3 \mu\text{m}$ hinges is modeled. Thicker hinges were used so that the saturation of the permalloy occurred over a broader range in the external magnetic field. This permits determining how well the model fits all regions of the device behavior.

It can be seen from Figs. 4 and 5 that the incorporation of the anisotropy torque in the model delays the steep rise in magnetization and inclination angle in comparison to the analysis without it. This verifies that the values for θ over this range of magnetic field strength are on the same order of magnitude as the demagnetization factor for the permalloy segment. This also shows that while further reduction of the demagnetization factor may shift the steep portion of the magnetization curve to lower background magnetic field levels, this phenomenon will begin to diminish once the demagnetization factors become negligible in comparison to the values of θ . Accurate agreement in the non-saturated region of the characteristic curve is vital, since when substrates restrict the angular range of the device to $\sim \pm 0.1$ rad incomplete magnetization will exist, and as the low field behavior requires more complex modeling. The data in Fig. 4 confirms that the shape demagnetization factor does not limit the magnetic susceptibility of the permalloy beam; instead it is limited by θ , which is virtually independent of the shape anisotropy (provided N_L is known to be $\ll 1$). Therefore, a maximal degree of shape anisotropy exists such that further increase in the permalloy aspect ratio produces no gain in magnetization, and, in fact, only reduces the available volume for Ni/Fe patterning, reducing the magnetic torque.

4.2. Measured device switching

Each of the three designs was also fabricated with optically transparent upper substrates so that appropriate testing could be performed while keeping the devices in view. Latching bistable behavior was observed for each of the three designs. The main point of interest is the minimum switching conditions required for operation of the devices, such as the minimum external field, B_{min} , that will produce latching, as well as the minimum current necessary to be supplied to the integrated coil in order to switch the state of the relay at the minimum external field. Note these currents are somewhat less than those reported in Table 1 of part 1 when these values were modeled at 10 mT for designs 1 and 3 and 25 mT for design 2. These parameters were previously modeled and appear in Table 1, along with their experimentally determined values. For example, the modeling for design 1 predicts a minimum 26 mA must be supplied to the coil with a minimum background magnetic field of 1.3 mT in order to produce switching between two latched states. Experimentally, the lowest value of this parameter was found to be 30 mA supplied to the coil with a background magnetic field of 1.5 mT, in good agreement with the modeled values. Additionally, this value of 30 mA gives an estimate of the coercive field strength, since the elastic torque is diminished by the demagnetization factor, and $B_{\text{external}} \sin \phi$ is small for device 1 in a 10 mT magnetic field. Design 2 is found to require a much greater minimum external magnetic field to produce latching bistable states [1]. This is due to the much lower degree of shape anisotropy, and thus a much lower degree of magnetization at a given external magnetic field level. Therefore a larger background field is necessary to generate a magnetic torque large enough to suitably overcome the elastic torque due to the bending hinges.

The effect of the external magnetic field on the minimum pulse width needed for a 50 mA coil current to produce a switching event was measured for a type-3 device. Fig. 6 shows that for external fields less than 12.7 mT (but greater than the minimum latching field) the minimum pulse length

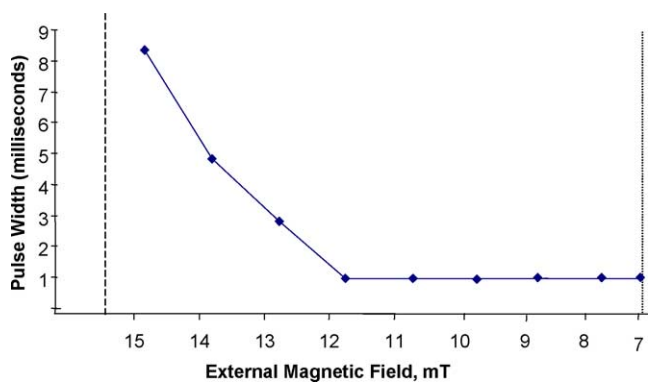


Fig. 6. Minimum pulse width necessary to switch type-3 devices not operating in SPS mode, shown as a function of the background external magnetic field.

needed to switch a type-3 device with a 50 mA current is 1.15 ms (note: 1.15 ms is not the total time to switch, but rather the length of time the current pulse need be provided to the coil for switching to result and does not take into account any under damping (ringing) in the latched state). This 1.15 ms pulse of 50 mA corresponds to a switching energy of 80 μJ . However, as the background magnetic field is increased, longer pulse widths were required. For example, at 15.0 mT, a pulse of over 8 ms was required. Once the background field exceeded 15.7 mT, a 50 mA pulse of indefinite length could no longer switch the device (a larger current was required). At this external field, the condition presented in Eq. (1) of Part 1 is no longer satisfied.

During testing it was observed that device 3 could be switched in one direction with millisecond pulse widths, but could be switched to the other direction with a pulse width shorter than 100 μs , confirming the SPS regime initially presented in [1]. This asymmetry could not be explained by the testing method or equipment; however, an explanation was found after consulting the model of this design developed in previous work [1]. It was observed that a current of 50 mA was needed to switch the devices in the short-pulse regime, as opposed to 35 mA for the long-pulse switch. Fig. 3 in Part 1 shows the magnetic field developed by the coil per unit of current supplied. For a type-3 device in a background field of 10 mT, the demagnetization can be dominated by the angle the magnetization vector, M , makes with the easy axis of the permalloy, θ , and not by the easy axis shape anisotropy factor, N_L . Furthermore, equating the magnetic torque to the anisotropy torque gives θ to be 0.0012 rad. Fig. 6 of Part 1 shows that the remaining elastic torque to be overcome is approximately 1 nNm, predicting a ΔB_{coil} of 0.15 mT. A coil current of approximately 10 mA would account for this ΔB_{coil} necessary for short-pulse switching (shown in the Section 2). The observed increase of 15 mA for short-pulse switching is in close agreement with the calculated value and supports the conclusion that little only a small degree of reversed magnetization needs to be developed during the application of the coil current to dramatically affect the permalloy coercivity. Therefore, no large increase in current is required to realize SPS for type-3 devices.

4.3. Contact resistance

The devices were placed in a background external field. The contact resistance across the devices was determined using a two-point measurement. A voltage generator supplied a square waveform to a potentiostat to produce the square current provided to the integrated coil. Typical values of the measured contact resistance were 0.5 Ω for new devices. Pulses varying in length from 1 to 10 ms were used to investigate the effect of switching speed on the switching of the various designs. Recorded contact resistance across the beam and microstrip also served to determine the effective switching speed of the MEMS devices (<5 ms).

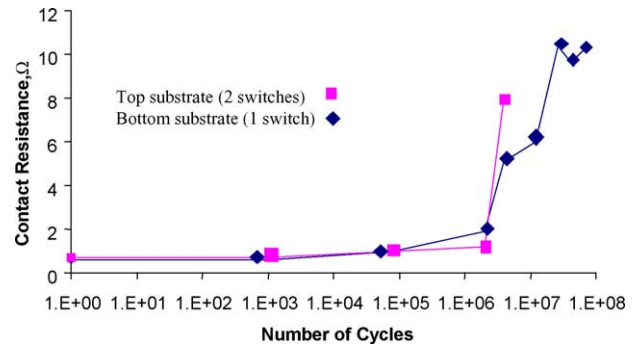


Fig. 7. Device lifetime testing: measured change in contact resistance with cycling for a type-2 device.

4.4. Cycling and lifetime tests

Several devices of each design were cycled in order to test for the lifetime electrical and mechanical performance. The contact resistance across the device was measured at several intervals, and the device was observed for any signs of wear of mechanical fatigue or failure, such as metal delamination or cracking. Fig. 7 shows the measured contact resistance of a transfer switch device of design 2 over 63 million cycles. Device cycling and testing occurred in an unpackaged state in ambient air. A DC current of 100 μA was applied in the latched states. The contact resistance was measured both in the upstate and the downstate. The upstate configuration connected two such switches across an RF transmission line on the upper substrate. The experimental resistance was divided by the number of switches in series 2, to give a resistance per MEMS switching element. Over the first 2 million cycles, little to no change is observed in the contact resistance of the RF switch, and values of 0.5–0.7 Ω are measured. The actual contact resistance should be somewhat less than this value due to the error incurred in using a two-point measurement. After 2 million cycles, the contact resistance in both states increased, rising to almost 10 Ω in the downstate after 27 million cycles. Reliable contact was not observed in the upstate at 12 million cycles. As the cycling continued no further increase in resistance was observed in the downstate. This abrupt increase in contact resistance could be due to particulate contamination (dust particles, etc.) since no attempt was made at hermetic sealing or packaging the device. After 63 million cycles, the contact resistance was similar to that at 27 million cycles. At this point, testing was stopped. The results in Fig. 7 are typical of what was observed with several samples. Testing the unpackaged devices in ambient conditions represents a worst-case scenario in evaluating performance and device lifetime. It is therefore believed that these devices would operate over many more cycles before deterioration of contact resistance when properly packaged and operated in a clean, dry environment. Devices of each design were subjected to further cycling in order to ascertain the mechanical lifetime. Mechanical cycling continued to 150 million cycles. No observable wear of material delamination

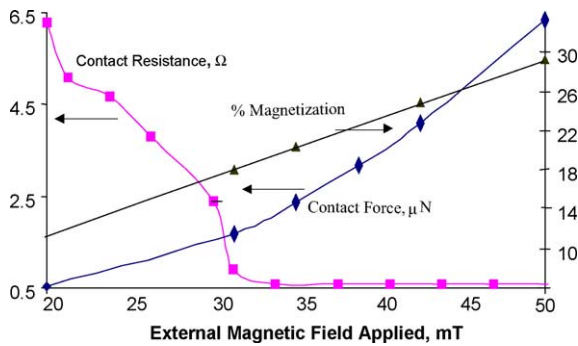


Fig. 8. Measured change in contact resistance with background magnetic field and comparison to modeled magnetization (expressed as %), and contact force (given in μN) for a type-2 device.

occurred, nor were the hinges found to experience a change in stiffness.

4.5. Contact force

It is well known that the force applied at the point of contact influences the quality of the contact between MEMS devices and the contact pads. Hosaka has demonstrated that a contact force in the range of $50 \mu\text{N}$ is necessary to achieve contact resistances less than $100 \text{ m}\Omega$ [5]. Experiments were performed on the magnetic actuators to determine the degree of benefit in contact resistance achievable through increased contact force. A device of design 2 was exposed to magnetic field levels in excess of the minimum required for latching, and the resistance across the device was measured using a two-point technique. After the beam makes initial contact with the pad at 14 mT , a high contact resistance (6.5Ω) is observed, as shown in Fig. 8. Increased background magnetic field levels, however, quickly reduce the measured contact resistance, dropping to 0.6Ω with a 30 mT magnetic field. This field level is calculated to correspond to a contact force in the $3 \mu\text{N}$ range. Further increase in background magnetic field level, and commensurate increase in contact force (up to $10 \mu\text{N}$ for design 2), was not observed to be of any further benefit in reducing contact resistance over this range in contact force. In this manner the operating field levels for the various device designs can be low enough to enable low switching energy, while high enough to benefit from greatly reduced contact resistance over this $0\text{--}3 \mu\text{N}$ range.

4.6. Overdriving

When devices were operated in magnetic fields stronger than the minimum latching magnetic field, movement of the beam tip along the substrate was observed for devices 1 and 3. This behavior is desirable in many cases as it provides an additional degree of freedom for the design engineer. In the case of the RF switch, overdriving the actuation coil in a sinusoidal fashion creates a wiping action in either of the latched states that tends to clean the contact surface leading to

higher quality electrical contacts. In the case of the microfluidic valve, the additional movement in the latched state could be used for regulating the amount of fluid passed through the device, or used in cytometry as a potential means of cell sorting. This capability was built-in to the design by nature of the long, flexible partial hinges. This effect was observed in devices 1 and 3 due to their enhanced magnetization, and therefore greater magnetic torque, in comparison to device 2 at similar background magnetic fields. Device 1 was observed to wipe a distance of approximately $50 \mu\text{m}$ in fields of 70 mT .

5. Discussion

The devices demonstrate these different modes of switching. All devices required at least a 1.2 ms pulse for switching in both directions with the exception of design 3. Design 3 required a 1.2 ms pulse of 50 mA for switching from the upstate to the downstate, but $100 \mu\text{s}$ at 50 mA was sufficient for switching from down to up. Below 40 mA , no pulse length produced switching from down to up. This supports the theory that a minimal pulse magnitude is necessary to switch from the lower latched state to the upper latched state, but that there is no minimal pulse time. Pulses shorter than $100 \mu\text{s}$ were not investigated, but it is believed that shorter pulses could be used to activate the beam.

The SPS phenomenon was not observed with the higher anisotropic permalloy patterned on design 1 or the lower anisotropic permalloy patterned on design 2. The SPS was not observed with design 2 because the separation of the two magnetic torque lines is very small since it scales with N^{-1} , where N is the demagnetization factor of the permalloy geometry [1]. Therefore, for design 2, there is only a very limited region of angles the beam can be rotated through, where the upper magnetic torque line lies above the elastic line while in the downstate; conversely, there is a very limited region where the lower magnetic torque line lies below the elastic line while in the upstate [1]. For design 3, the separation of the two magnetic torque lines is greatest, but the slope of the magnetic torque line is also proportional to N^{-1} . If the elastic torque line were perfectly flat ($k_\phi = 0$), then this design would correspond to the same angular range where low energy switching may occur. For identically sloped elastic torque curves with the same initial inclination angle, the angular range for this effect is diminished. It can be seen that matching the stiffness of the hinge to the permalloy anisotropy could enhance the angular range over which low energy switching is observed. Increasing the stiffness of the hinge in design 1 would yield this effect for switching in both directions [1]. The compromise for low energy switching is reduced contact force, as the increased hinge stiffness requires a greater fraction of the magnetic torque for bending. This technology could be used in RF relays, as well as optical switches where contact force has a less critical role.

5.1. Applications

There are many applications for low energy, bistable magnetic actuators, including some that are complemented by the design and materials choices presented here. For cryogenic and/or higher-temperature applications, thermal stresses become significant. For MEMS devices to be used in extreme temperature environments, it is essential to choose materials that have similar coefficients of thermal expansion. In addition, thermal stresses may be further reduced by canceling thermally induced bending by cladding the magnetic material in gold, as described in the Section 3.

In addition to maintaining an improved, clean electrical contact, the wiping observed may also be employed for other applications, including microfluidics. The wiping movement is well suited for use as a variable-flow rate valve. Devices which demonstrate this wiping behavior are currently being investigated and will be the subject of a future publication.

MEMS concepts can also be applied to RF, replacing traditional solid-state components such as PIN diodes and FETs that are inherently nonlinear, are poor at power handling, and consume larger amounts of DC power. This is especially evident in communications applications where, in some cases, a single MEMS component replaces and outperforms an entire solid-state circuit [6]. RF MEMS alternatives offer lower power consumption, excellent linearity, better isolation, lower insertion loss, and increased functionality in applications where a high degree of frequency agility and sharp filtering is critical. A SPDT switching element could be used as a building block for a more complex switching network. For example, a tunable RF filter could be made by switching individual capacitive elements in and out with such a switch. SPDT switches can also be used in phase shifters to alter the phase length of a transmission line by switching sections of differing lengths in and out of the circuit. Fig. 9 is a schematic of a SPDT switch built using the fabrication steps

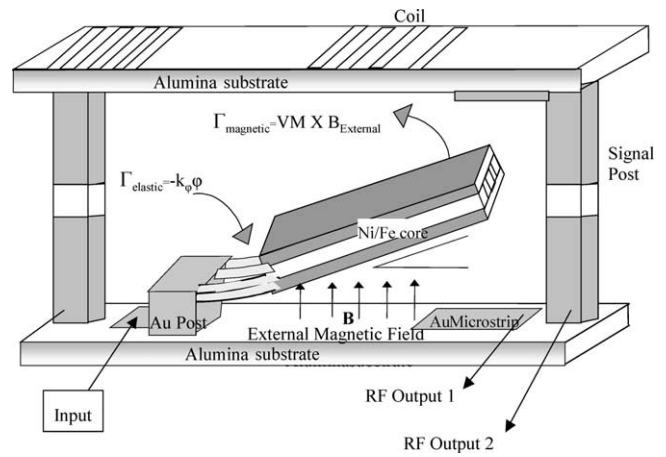


Fig. 9. Schematic of two-substrate actuator design with flexible hinges and stiff permalloy magnetic element.

described in this paper. The design utilizes the magnetic bistability described by Ruan et al. [2]; however, this design makes use of the short-pulse switching, utilizes a post platform for reduced mechanical stress at the hinge, and minimizes thermal stresses by cladding the ferromagnetic material in gold, therefore reducing deformation in cryogenic environments.

The SPDT design described in this study is well suited for these types of applications because there are no dead legs in the design. Device isolation is a critical measure of RF performance and is predominantly determined by the magnitude of the separation between the two RF outputs. Fig. 10 shows a family of curves which demonstrate the modeled isolation achieved between two microstrip transmission lines on opposing substrates which are separated by various gap distances. The model suggests that in order to achieve isolation better than -50 dB over the range of 500–2000 MHz, a substrate separation of approximately 100 μm is necessary. Fig. 11 shows the measured isolation across the transfer switch (two

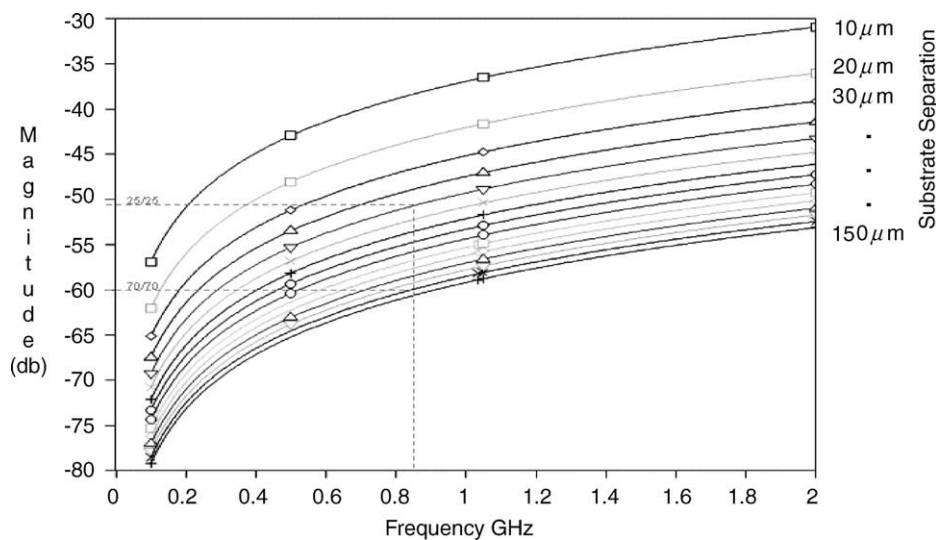


Fig. 10. Modeled isolation achieved with two-substrate design as a function of the total substrate separation.

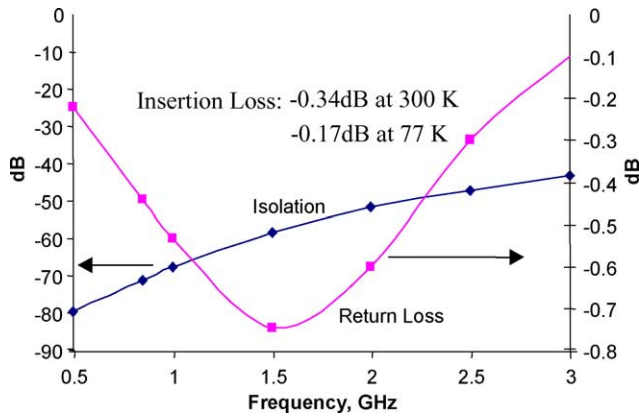


Fig. 11. RF performance of a fabricated MEMS transfer switch composed of two type-2 actuators: measured isolation, return loss, and insertion loss data for two-switch in series device.

switches in series). The isolation for the network is shown to be better than -50 dB across the entire band. The cantilever hinges were designed to be suitably flexible so that an external magnetic field of 10 mT could activate the switch, yet thick enough to be RF transmissive. In order to verify the temperature independence of the device, the insertion loss was monitored as the device was cooled from room temperature down to cryogenic temperature (77 K). Insertion loss of -0.34 dB was measured at 300 K and improved to -0.17 dB at 77 K as was expected for the transfer switch. With further design iterations, both isolation and insertion loss could be improved by impedance matching.

6. Summary

Three variations of SPDT MEMS RF switches were fabricated and tested for minimal switching energy, as well as electrical and mechanical reliability. Fabricated devices were found to have excellent correspondence between observed and modeled behavior. Isolation better than -50 dB was observed over the 500–2000 MHz range with insertion loss better than -0.2 dB. The design space for SPS was determined using the comprehensive model for this two-substrate doubly latching design. New designs were explored for minimum switching energy. It was found that magnetic torque curves that remain bounded by the elastic torque curve over the entire angular range of motion yield SPS. The coercivity of the magnetic material is critical in producing useful SPS behavior, even if the magnetic material is patterned in such a way as to maximize the magnetic susceptibility (through lithographic patterning of the Ni/Fe). Very low ferromagnet coercivity yields bistable actuation with minimal magnetization and very low contact forces. Hard magnetic materials with large coercivity produce a high degree of magnetization in the latched states, but require much larger currents

be provided to enable switching, greatly increasing the energy expended. The coercivity of the ferromagnet is of great importance in generating a design satisfying the necessary contact forces and energy requirements. Actuator displacements of $100 \mu\text{m}$ were observed repeatedly with switching energies of $5 \mu\text{J}$ from a $100 \mu\text{s}$ pulse of 50 mA. Further reduction in switching energy is anticipated, but shorter pulses were not investigated.

Acknowledgments

Significant contributions by Balam A. Willemsen and Jürgen Musolf of Superconductor Technologies, Inc. in the form of technical insight and valuable discussion are greatly appreciated. This material is based upon work supported by the Defense Advanced Research Projects Agency, Defense Science Office, DARPA Order No. J607 Total Agile RF Sensor Systems (TASS) issued by DARPA/CMD under Contract No. MDA972-00-C-0010.

References

- [1] G. Gray, P. Kohl, Magnetically Bistable Actuator. Part I: Ultra-low Switching Energy and Modeling, *Sens. Actuators A* 119 (2005) 489–501.
- [2] M. Ruan, J. Shen, C. Wheeler, Latching electromagnetic relays, *J. Microelectromech. Syst.* 10 (2001) 511–517.
- [3] C. Ahn, M. Allen, A fully integrated surface micromachined magnetic microactuator with a multilever meander magnetic core, *J. Microelectromech. Syst.* 2 (1993) 15–22.
- [4] J. Judy, R. Muller, Magnetically actuated, addressable microstructures, *J. Microelectromech. Syst.* 6 (1997) 249–256.
- [5] Hosaka, *Micro Electro Mechanical Systems*, 7–10 Feb. 1993, IEEE, Fort Lauderdale, FL, 1993.
- [6] J.J. Yao, RF MEMS from a device perspective, *J. Micromech.* 10. (2000) 9–38.

Biographies

Gary D. Gray Jr. received the BS degree in chemical engineering from the Georgia Institute of Technology, Atlanta, in 2000. He is currently working toward the MS degree in physics and the PhD degree in chemical engineering at the same.

Eric M. Prophet received his BS in Aerospace Engineering from UCLA in 1998 and an MS in Mechanical Engineering from UCLA in 2000. He is currently employed as a device physicist working on cryogenic MEMS devices at Superconductor Technologies Inc.

Lingbo Zhu is a graduate student at the Georgia Institute of Technology.

Paul A. Kohl received a BS degree in chemistry from Bethany College in 1974 and PhD from The University of Texas at Austin in 1978. He was employed by AT&T Bell Laboratories from 1978 to 1989 and joined the Georgia Institute of Technology in 1989, where he is now a Regents' Professor.